

Comparative study of *in vitro* apatite-forming abilities of highly ordered rutile nanorod arrays fabricated on cpTi and Ti6Al4V alloys

Xingzhu Liu, Tomohiko Yoshioka & Satoshi Hayakawa

To cite this article: Xingzhu Liu, Tomohiko Yoshioka & Satoshi Hayakawa (2019): Comparative study of *in vitro* apatite-forming abilities of highly ordered rutile nanorod arrays fabricated on cpTi and Ti6Al4V alloys, Journal of Asian Ceramic Societies, DOI: [10.1080/21870764.2019.1699230](https://doi.org/10.1080/21870764.2019.1699230)

To link to this article: <https://doi.org/10.1080/21870764.2019.1699230>



© 2019 The Author(s). Published by Informa UK Limited, trading as Taylor & Francis Group on behalf of The Korean Ceramic Society and The Ceramic Society of Japan.



Published online: 02 Dec 2019.



Submit your article to this journal [↗](#)



Article views: 92



View related articles [↗](#)



View Crossmark data [↗](#)

Comparative study of *in vitro* apatite-forming abilities of highly ordered rutile nanorod arrays fabricated on cpTi and Ti6Al4V alloys

Xingzhu Liu^a, Tomohiko Yoshioka^b and Satoshi Hayakawa^b

^aBiomaterials Laboratory, Graduate School of Natural Science and Technology, Okayama University, Okayama, Japan; ^bBiomaterials Laboratory, Graduate School of Interdisciplinary Science and Engineering in Health Systems, Okayama University, Okayama, Japan

ABSTRACT

The surfaces of commercially available pure titanium (cpTi) and Ti6Al4V alloy specimens were modified to form highly ordered rutile nanorod arrays by chemical treatment and subsequent aging treatment. The densities of the rutile rods were $(1.04 \pm 0.06) \times 10^3$ and $(0.70 \pm 0.10) \times 10^3 \mu\text{m}^{-2}$ for the cpTi and Ti6Al4V alloy specimens, respectively. Both the rutile nanorod arrays on the cpTi and Ti6Al4V alloy specimens deposited apatite particles when soaked in simulated body fluid (SBF) for one day. After soaking for various other periods, scanning electron microscopy images and thin-film X-ray diffraction patterns of these specimens showed that the cpTi specimens exhibited a superior rate of apatite nucleation and favored the formation of numerous apatite particles with larger diameter. This superior apatite-forming ability of the cpTi specimens can be attributed to the dense, thick titania layers with higher rutile nanorod density on their surfaces.

ARTICLE HISTORY

Received 11 August 2019
Accepted 11 November 2019

KEYWORDS

Rutile; nanorod arrays;
apatite; rod density


1. Introduction

Hydroxyapatite (HA) ceramics can bond spontaneously to living bone. They can be used to produce coating layers on metallic biomaterials for orthopedic and dental implants to integrate with bony tissues in the human body [1–3]. The coating layers prepare metallic implants with excellent mechanical properties to exhibit appropriate biocompatibility in the body environment. Various surface modification processes [4–7], such as the sol-gel method [5], electron-beam deposition [6], and thermal spraying treatment [7], have been reported to prepare HA layers on the surfaces of various metallic biomaterials such as titanium or its alloys. At the same time, *in vitro* deposition of bone-like apatite layers on the surfaces is a widely employed approach to evaluating the bioactivity of implants [8–10].

Metallic implants made of commercially available pure titanium (cpTi) and its alloys (Ti6Al4V) are currently employed for dental and orthopedic applications. Some previous reports have shown that titania layers coating titanium and its alloys induce apatite deposition in Kokubo's simulated body fluid (SBF). This fluid has inorganic ion concentrations similar to those in human blood plasma [11]. Shozui et al. [12,13] prepared titania layers on various substrates using the sol-gel method and found that their *in vitro* apatite-forming ability depended on the substrates. Hayakawa et al. [14] examined the effects of an Al substrate and Ti6Al4V alloys on the nucleation and growth of apatite in SBF and reported that aluminum species released

into the SBF from the Al substrate or Ti6Al4V alloys were responsible for inhibiting apatite nucleation on the surface of the titania layers. In an earlier report, they applied a liquid-phase-deposited titania coating to Ti6Al4V alloy substrates in order to reduce the inhibiting effect of aluminum species derived from the substrates on apatite nucleation [15]. Properly designed gaps (GRAPE technology [15,16]) were also required, however, to enable *in vitro* apatite deposition on the titania coating. If the titania coating deposited in the liquid phase is too thin, the inhibiting effect of the aluminum species derived from the substrates may not be sufficiently mitigated. Thus, titania coatings exhibit a low apatite-forming ability in conventional SBF solutions.

Most recently, the importance of a rutile layer has been emphasized in inducing apatite formation *in vitro* [17,18]. This is because numerous oxygen atoms are present on specific facets of rutile. As reported by Xiao et al. [18], the small lattice mismatch between the oxygen atoms on specific facets of rutile and apatite may be an important factor influencing the *in vitro* apatite-forming ability. In addition, Wu et al. [19] proposed that a complicated surface morphology and nanosized rutile crystallites can contribute to effectively inducing apatite formation *in vitro*. According to Rohanizadeh et al. [20], a rutile layer produced by H₂O₂ oxidation and subsequent heat treatment for 30 min can induce deposition of more apatite particles than are produced using a longer

CONTACT Satoshi Hayakawa  satoshi@cc.okayama-u.ac.jp  Biomaterials Laboratory, Graduate School of Interdisciplinary Science and Engineering in Health Systems, Okayama University, 3-1-1 Tsushima, Kita-ku Okayama 700-8530, Japan

© 2019 The Author(s). Published by Informa UK Limited, trading as Taylor & Francis Group on behalf of The Korean Ceramic Society and The Ceramic Society of Japan. This is an Open Access article distributed under the terms of the Creative Commons Attribution License (<http://creativecommons.org/licenses/by/4.0/>), which permits unrestricted use, distribution, and reproduction in any medium, provided the original work is properly cited.

heating period (90 min). They also indicated that rutile layers exhibit excellent adhesion strength with apatite layers.

Recently, a few studies [17,18] have reported that titania rods can induce the formation of apatite on their surfaces in SBF. Our previous report [17] described successful preparation of titania rods consisting of anatase and rutile, and reported their deposition of apatite particles when soaked for 3d in SBF. However, the effects of the rod structures on apatite deposition were not examined and discussed in previous studies. As the above suggests, further work is still required to obtain a detailed understanding of the mechanisms by which nucleation and growth of apatite are induced on rutile rods.

We have recently reported that dense, thick rutile layers can be successfully prepared on the entire surface of a cpTi substrate [21]. If the entire surface of a Ti6Al4V alloy substrate can be coated with dense, thick rutile layers, the release of Al from the Ti6Al4V alloy substrate into the SBF can be inhibited, thereby benefiting the nucleation and growth of apatite on rutile layers in a conventional SBF. In the present work, cpTi and Ti6Al4V alloy discs were subjected to chemical treatment as described in our previous paper [21] to obtain rutile nanorod arrays on their surfaces. The nucleation and growth behavior of apatite on the rutile nanorod arrays obtained on the cpTi and Ti6Al4V alloy discs were compared for the discs soaked in SBF for various periods. The possible factors affecting apatite deposition on rutile nanorod arrays fabricated on cpTi and Ti6Al4V alloy substrates were explored.

2. Materials and methods

2.1. Fabrication of rutile rods on cpTi and Ti6Al4V alloys

Titanium discs (15Φ × 1 mm) were purchased from GC Corp. (Tokyo, Japan) and Ti6Al4V alloy discs (12Φ × 1 mm) were purchased from Teijin-Nakashima Medical Co. Ltd. (Okayama, Japan). The discs were polished using SiC (#1000) abrasive sandpaper to prepare smoother substrates, and then cleaned ultrasonically in ultra-pure water and acetone for 5 min. The cleaning cycle was repeated three times. Rutile nanorod arrays were fabricated on the cpTi and Ti6Al4V alloy discs according to the methods described in our previous reports [21]. In brief, each cpTi or Ti6Al4V alloy disc was each soaked in 30 mL of treatment solution (TS, pH 0.7) at 80°C for 3 d. The TS contained 0.14 mol·m⁻³ TiOSO₄ (Maikun Chemical Company, Shanghai, China), 15 mol·m⁻³ hydrogen peroxide (H₂O₂), and nitric acid (HNO₃). After soaking in TS for 3 d, the samples were washed ultrasonically in ultra-pure water for 15 min, and then soaked in 30 mL of ultra-pure water at 80°C

for 1 d as aging treatment. Subsequently, the samples were dried in air at room temperature and denoted as CT-specimens (CT-cpTi and CT-Ti6Al4V).

2.2. In vitro evaluation of the ability to induce apatite deposition

Kokubo's SBF with an ion concentration similar to that of human blood plasma was prepared as described in the literature [11]. Reagent-grade chemicals comprising NaCl, NaHCO₃, KCl, K₂HPO₄·3H₂O, MgCl₂·6H₂O, CaCl₂, and Na₂SO₄ were sequentially dissolved in ultra-pure water. (CH₂OH)₃CNH₂ and 1 mol·dm⁻³ HCl were used to adjust the pH to 7.4. The ability to induce apatite deposition on the samples prepared according to section 2.1 was evaluated by soaking them in 40 mL of SBF at 36.5°C for various periods. After soaking in SBF, both sides of the samples were gently washed with ultra-pure water and dried in air at room temperature.

2.3. Structural characterization

The crystalline phases of the prepared samples before and after soaking in SBF were characterized by thin-film X-ray diffraction (TF-XRD, X'Pert-ProMPD, PANalytical, Almelo, the Netherlands: Cu Kα, λ = 0.15418 nm, 45 kV –40 mA). The TF-XRD patterns were measured in the step-scan mode with a constant X-ray incident angle θ of 1.0°. The surface morphology of the prepared samples was examined by field-emission scanning-electron microscopy (FE-SEM; JSM-6701F, JEOL, Ltd., Tokyo, Japan). The samples were covered with high-purity osmium for FE-SEM observation with a Neoc-STB osmium coater (Meiwafosis Co., Ltd., Tokyo, Japan). FE-SEM analysis was also conducted to determine the density of the nanorod arrays. The rod density of the nanorod arrays is defined as the number of nanorods per square micron on the surface. At least 15 small images with an area of 1 × 1 μm² were chosen stochastically from the FE-SEM images, and the number of nanorods in each image was then collected for calculating the average rod density of each sample. Scanning electron microscopy (SEM; VE-9800, Keyence Corp., Osaka, Japan) was used to examine the surface morphology of the samples after soaking in SBF for various periods. Before the SEM observation, the samples were coated with a platinum-palladium coating (thickness: 10 nm) using a sputter coater (Ion Sputter E-1030, Hitachi High-Technologies Co., Ltd., Tokyo, Japan). The SEM images were analyzed using ImageJ software (version 1.51, Wayne Rasband, NIH, Bethesda, MD, USA) to determine the quantity, size, and surface coverage of the deposited apatite particles.

3. Results

Figure 1 shows FE-SEM images of the CT-cpTi and CT-Ti6Al4V specimens. The low-magnification images

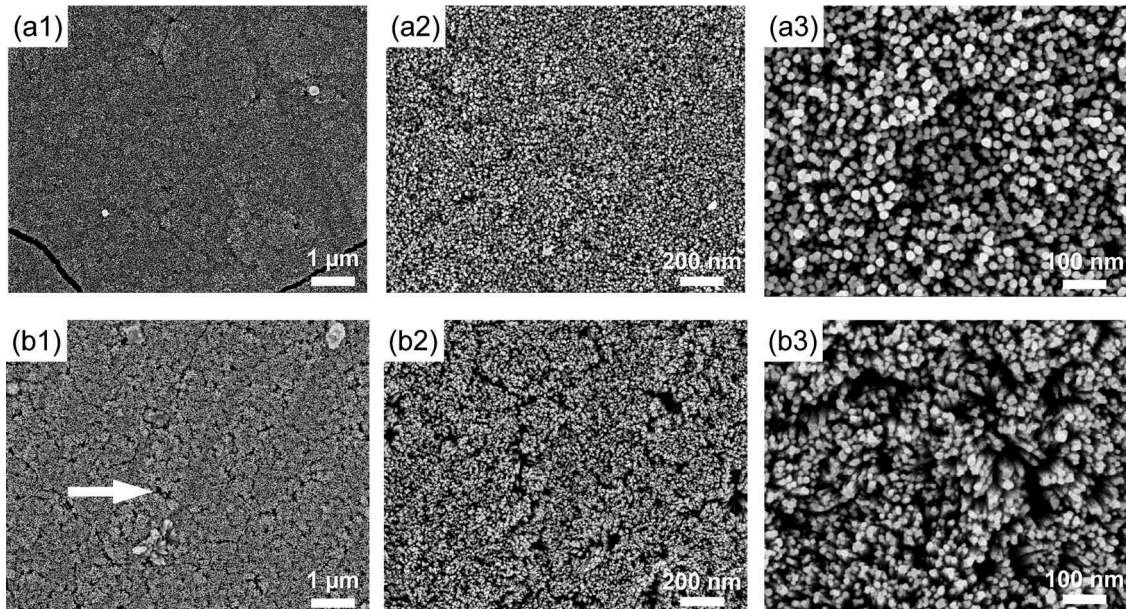


Figure 1. FE-SEM images of CT-cpTi (a1: $\times 10k$, a2: $\times 30k$, a3: $\times 100k$) and CT-Ti6Al4V (b1: $\times 10k$, b2: $\times 30k$, b3: $\times 100k$) specimens.

(Figure 1(a1, b1)) show dense, rough nanorod arrays formed on both samples. Dense nanorod arrays were further confirmed on the CT-cpTi specimen in Figure 1(a2). Comparing Figure 1 (a1, b1), we can see that the nanorod arrays formed on the CT-Ti6Al4V specimen were relatively loose, with some pores and gaps on their surfaces (white arrow). The evaluated diameter of some pores and gaps was 100 – 250 nm (Figure 1 (b2)). A closer look at two characteristic surfaces (Figure 1(a3, b3)) shows that that these layers were made up of rod-like structures. The estimated width of the rods was approximately 21 – 25 nm for the CT-cpTi specimen and approximately 14 – 20 nm for the CT-Ti6Al4V specimen. Although slightly inclined, these rods grew in the same direction in the CT-Ti6Al4V specimen. This indicates that the CT-cpTi substrates favored the formation of larger nanorods. The rod density for the CT-cpTi and CT-Ti6Al4V specimens was calculated from high-magnification SEM images (Figure 1(a3, b3)). The densities of the rods on the CT-cpTi and CT-Ti6Al4V specimens were approximately $(1.04 \pm 0.06) \times 10^3$ and $(0.70 \pm 0.10) \times 10^3 \mu\text{m}^{-2}$.

This indicates that the nanorods formed on the CT-cpTi specimen were much denser than those formed on the CT-Ti6Al4V specimen.

Cross-sectional backscattered electron (BSE) SEM images of the CT-cpTi and CT-Ti6Al4V specimens in 0.14 mol·m⁻³ TS after aging treatment are shown in Figure 2. A boundary line can be confirmed in the middle of the figure. The upper part of the figure is the formed layer, and the bottom part is the metallic substrate. A significant difference in the cross-sections is seen in the thicknesses of the layers. The layer formed on the CT-cpTi specimen was approximately 1.8 – 2.6 μm thick, while a thinner layer of 1.4 – 1.7 μm was observed on the surface of the CT-Ti6Al4V specimen.

Figure 3(a) shows TF-XRD patterns of the samples after chemical treatment and subsequent aging treatment. The CT-cpTi and CT-Ti6Al4V specimens exhibit diffraction peaks at 2θ angles of approximately 27°, 36°, and 38°, corresponding to diffraction from the (110), (101), and (111) planes, respectively, of rutile titania (ICDD-JCPDS PDF#21-1276). The remaining

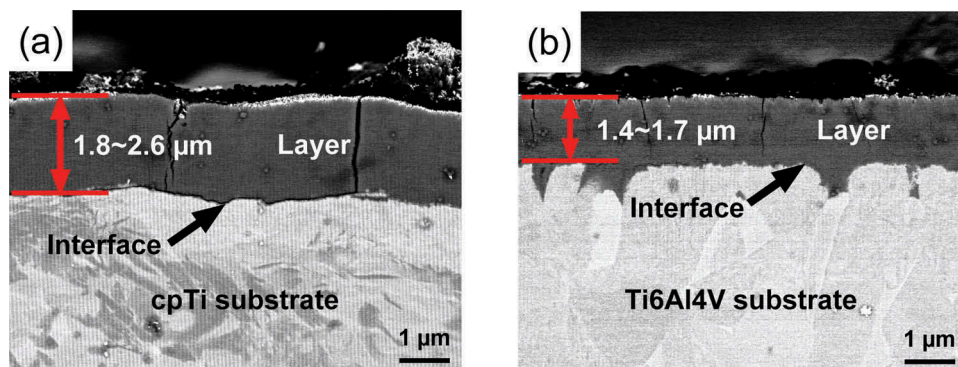


Figure 2. Cross-sectional BSE-SEM images of (a) CT-cpTi and (b) CT-Ti6Al4V specimens.

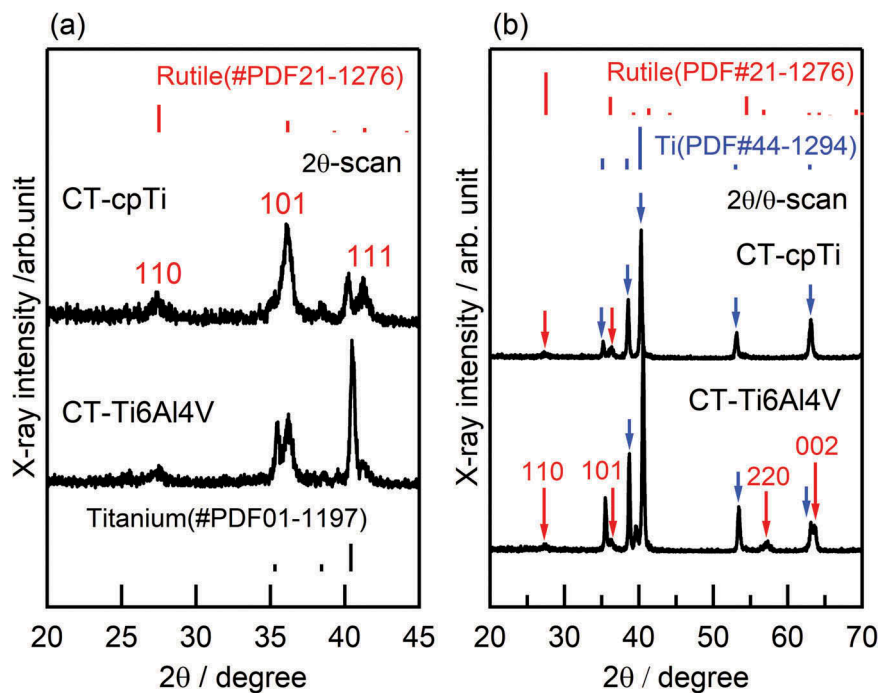


Figure 3. (a) TF-XRD patterns and (b) XRD patterns in $2\theta/\theta$ scan mode of CT-cpTi and CT-Ti6Al4V specimens.

peaks are consistent with the diffraction peaks of metallic substrates. This indicates that the titania layers consisted of the pure rutile phase. In addition, the intensities of the (101) planes of rutile on the CT-cpTi specimen were stronger than those of rutile on the CT-Ti6Al4V specimen. To confirm the preferred orientation of rutile layers fabricated on CT-cpTi and CT-Ti6Al4V specimens, XRD patterns of CT-cpTi and CT-Ti6Al4V specimens obtained in the $2\theta/\theta$ scan mode are shown in Figure 3(b). It is notable that both CT-cpTi and CT-Ti6Al4V specimens showed similar diffraction peaks at 27° , 36° and 63° corresponding to (110), (101) and (002) planes of rutile. In addition, a diffraction peak at 57° ascribable to the (220) plane of rutile can be observed on the CT-Ti6Al4V specimen. The other diffraction peaks were assignable to α -Ti. The relative diffraction intensities of peaks on the (101) and (110) rutile planes ($I_{(101)}/I_{(110)}$) of Figure 3(b) was calculated. The $I_{(101)}/I_{(110)}$ values for CT-cpTi and CT-Ti6Al4V alloy substrates were 2.6 and 2.3, respectively, which are higher than the ($I_{(101)}/I_{(110)} = 2.2$) presented in the previous study [18]. In addition, the diffraction intensities of the (002) planes of rutile on CT-cpTi and CT-Ti6Al4V alloy substrates were stronger than those on the other planes of rutile. These results indicated that the rutile layers were forced to grow along the c -axis.

Figure 4 shows TF-XRD patterns of the CT-cpTi and CT-Ti6Al4V specimens after soaking in SBF for various periods. The diffraction peaks at $2\theta = 25^\circ$ and 32° correspond to apatite (ICDD-JCPDS PDF#09-432). It can be seen that the intensity of the diffraction peaks of apatite increased with the soaking time in SBF. Figure 4(a) shows that the soaking time required for detecting the diffraction peaks of apatite is 30 h for the

CT-cpTi specimen. On the other hand, it took at least 48 h for the CT-Ti6Al4V alloy specimen to show apatite diffraction peaks. In addition, the intensity of the diffraction peak at approximately 32° , corresponding to apatite, was stronger on the CT-cpTi specimen than on the CT-Ti6Al4V specimen soaked for 72 h. The induction period for apatite formation should be further confirmed via SEM images, however, due to the limited sensitivity of the TF-XRD measurements of the samples after a short immersion in SBF.

Figure 5 indicates the surface morphology of the samples before and after immersion in SBF for various periods. After soaking in SBF for 12 h, small hemispherical particles (1 – 2 μm diameter) appeared on the surface of the CT-cpTi and CT-Ti6Al4V specimens, which implies that those particles were deposited within 12 h of soaking. Nevertheless, the CT-Ti6Al4V specimens developed a smaller number of particles on the surface than the cpTi discs within 12 h of soaking. The diameters of the particles formed on the CT-Ti6Al4V specimen are also smaller than on the CT-cpTi specimen. After 24 h of soaking in SBF, more hemispherical particles, which were identified as apatite by TF-XRD analysis, formed on the surfaces of both specimens (Figure 4).

Figure 6(a) shows the diffraction peak area at 32° for use in estimating the amount of apatite particles deposited on the sample surface. This peak corresponds to the apatite calculated from the TF-XRD patterns of Figure 4 as a function of soaking time. In Figure 4, the peak area on the CT-Ti6Al4V specimen was corrected by considering the apparent surface area of the CT-cpTi and CT-Ti6Al4V specimens. The CT-cpTi and CT-Ti6Al4V specimens showed similar growth

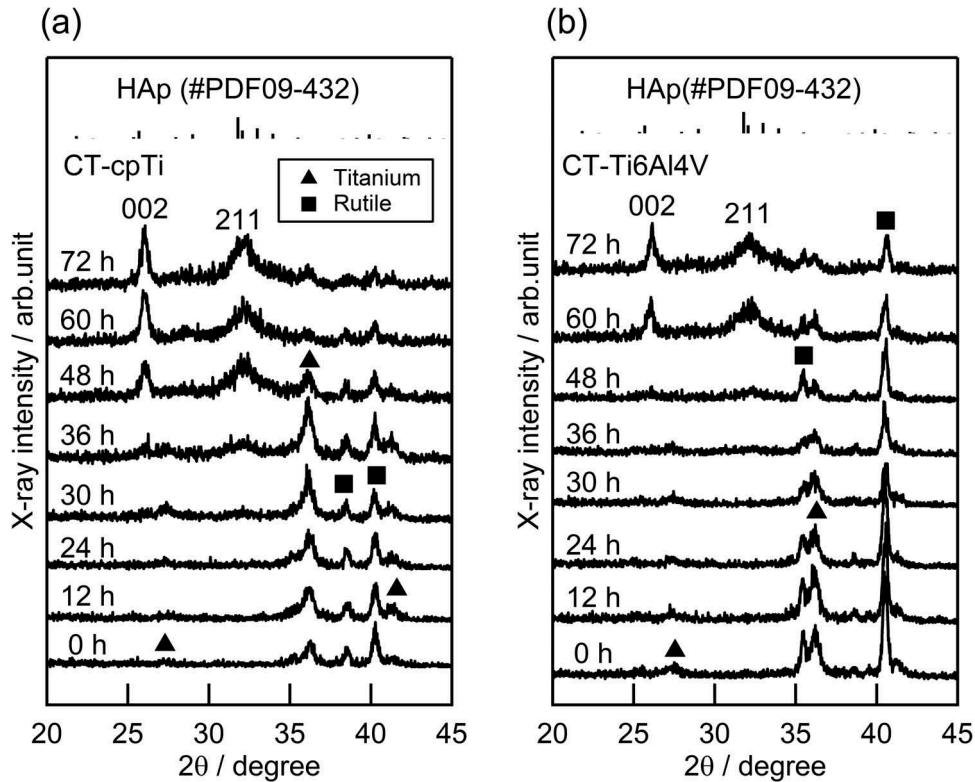


Figure 4. TF-XRD patterns of (a) CT-cpTi and (b) CT-Ti6Al4V specimens before and after being soaked in SBF at 36.5°C for various periods up to 72 h.

curves for the amounts of apatite particles. The estimated time required to induce apatite deposition was 12 – 24 h for the CT-cpTi specimen and 30 – 36 h for the CT-Ti6Al4V specimen. This indicates that the rutile layers on the CT-Ti6Al4V specimen delayed the induction of apatite deposition.

On the basis of the SEM observation (Figure 5), the number and size of the hemispherical apatite particles on the CT-cpTi and CT-Ti6Al4V specimens were plotted as a function of soaking time in the range of 0 – 72 h in Figure 6(b, c). Both samples exhibited similar monotonically increasing behavior of the particle number. There were more apatite particles on the CT-cpTi specimen than on the CT-Ti6Al4V specimen throughout the soaking time in SBF. Although there was no significant difference in the size of the apatite deposited on the surfaces of the CT-cpTi and CT-Ti6Al4V specimens in Figure 6(c), the slope of the curve for the CT-cpTi specimen was slightly steeper than that for the CT-Ti6Al4V specimen. The number and size of the hemispherical apatite particles increased with the soaking time in the range from 0 h to 40 h. (Figure 6(b, c)) This implies that the primary and secondary nucleation and growth of apatite occurred up to 40 h.

In Figure 6(d), the number of apatite particles is plotted as a function of coverage. Although the number of deposited apatite particles was different, the CT-cpTi and CT-Ti6Al4V specimens both exhibited similar increasing behavior. The CT-cpTi specimen reached

a plateau at about 35% coverage, while the CT-Ti6Al4V specimen plateaued at about 45% coverage. The curve in Figure 6(d) shows a monotonic increase in the number of particles in the 0–40% coverage range due to the primary and secondary nucleation and growth of apatite, followed by a plateau stage due to the secondary nucleation and growth of apatite.

4. Discussion

Regardless of the surface morphology of the substrates subjected to chemical and aging treatments, apatite was formed on both the CT-cpTi and CT-Ti6Al4V specimens in SBF within three days. Takadama et al. [22] reported treatment of a Ti6Al4V alloy substrate with NaOH solution to induce apatite deposition in vitro after soaking in SBF for 120 h. They indicated that Ti-OH groups, which are important for in vitro apatite nucleation, were formed on the surface due to the exchange between Na ions on the Al and V-free sodium titanate layer and H_3O^+ in the SBF. They described a similar process of apatite deposition on Ti with NaOH treatment [23]. The ability to induce apatite deposition on Ti6Al4V alloys with mixed acid treatment followed by heat treatment has, moreover, been discussed by Yamaguchi [24]. The author reported that the treated Ti6Al4V alloys did not form apatite in SBF within three days. In contrast, the results in our work demonstrated that rutile arrays on CT-cpTi

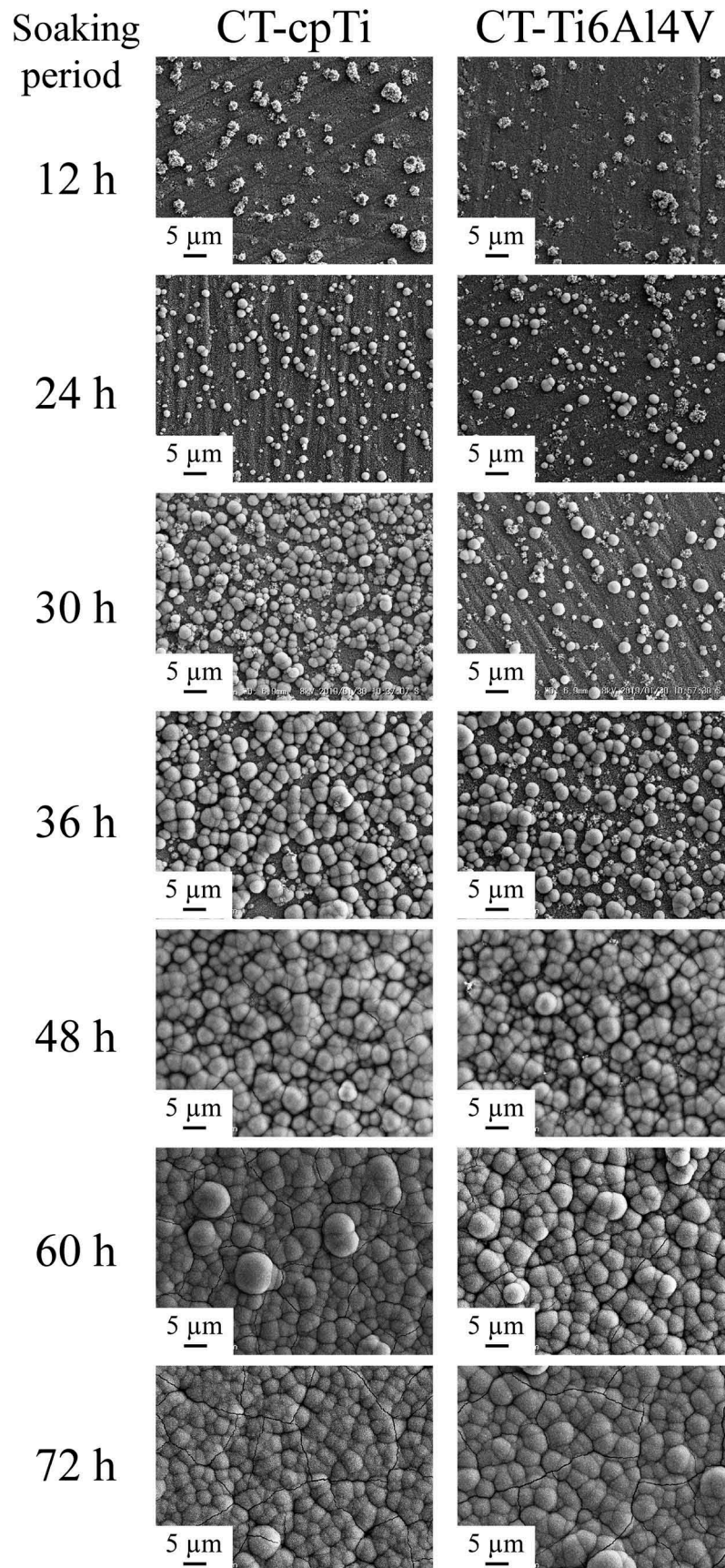


Figure 5. SEM images of the surfaces of CT-cpTi and CT-Ti6Al4V specimens after soaking in SBF at 36.5°C for various periods.

and CT-Ti6Al4V specimens are useful for inducing apatite deposition in SBF within one day. It is also important to note that the behavior of apatite formation differed on the CT-cpTi and CT-Ti6Al4V specimens.

As reported by Uchida et al. [25], apatite was formed on titania layers because the atomic oxygen arrangements in titania crystal structures were suitable for epitaxy of the hydroxyl groups of apatite crystals in SBF. Xiao

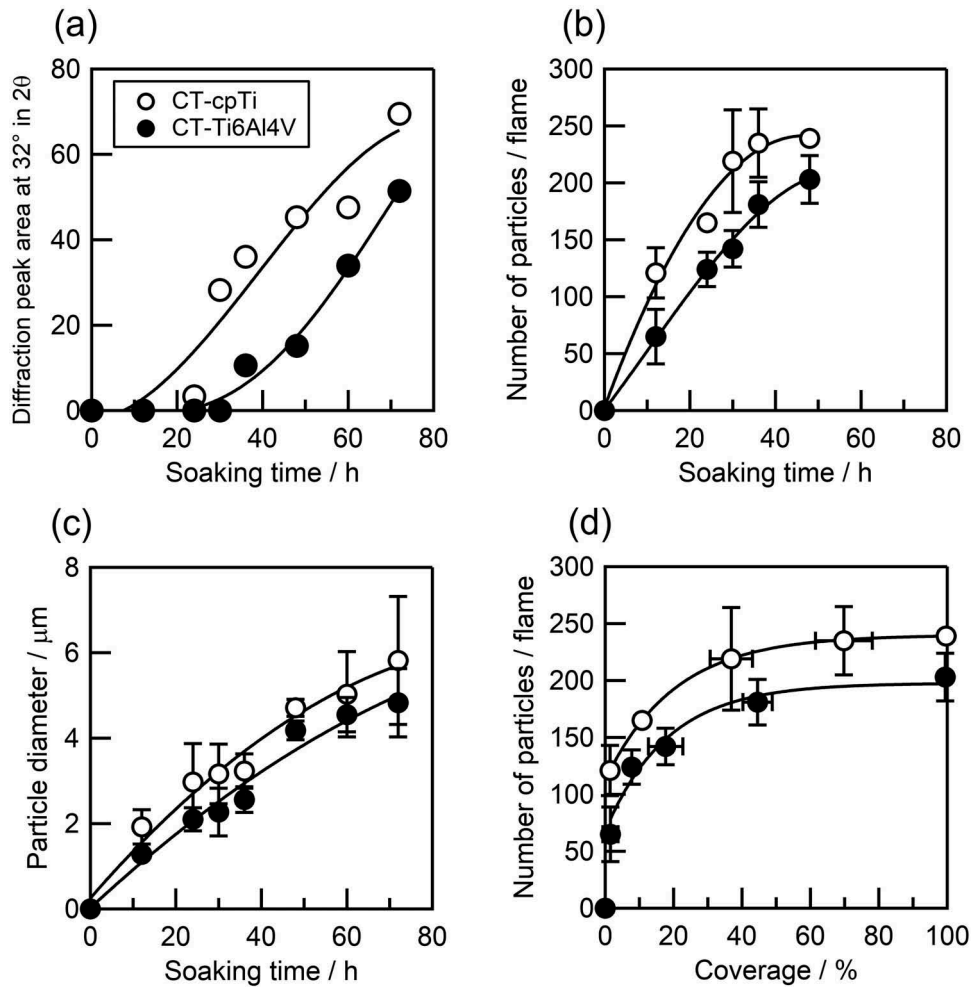


Figure 6. (a) Thin-film X-ray diffraction peak area at $2\theta = 32^\circ$ corresponding to apatite, (b) the number of deposited apatite particles, and (c) the average diameter of deposited apatite particles, as a function of soaking time in SBF. (d) The number of apatite particles is plotted as a function of coverage, which is the fraction of the surface covered by the apatite particles.

et al. [17] have emphasized the importance of crystal lattice matching between rutile or anatase layers and apatite in inducing apatite formation in SBF. On the other hand, Li et al. [26] have proposed that the apatite-forming ability of titania layers in vitro is owing to the presence of Ti–OH groups on the surface. They highlighted the associated responsibility of the negatively charged surface as well as the number of Ti–OH groups in inducing apatite formation. Uetsuki et al. [27] revealed that Ti–OH groups would exist on titania layers in two kinds of states, acidic and basic. In other words, titania surfaces support the coexistence of positively charged Ti–OH₂⁺ and negatively charged Ti–O[−] when exposed to SBF. The arrangement of Ti–OH₂⁺ and Ti–O[−] sites on the surface determined the surface charge density, surface energy, and primary apatite nucleation. Ti–OH₂⁺ sites and Ti–O[−] sites on the titania surface were expected to accept the positive (calcium) and negative (phosphate) ions of SBF to form an apatite nucleus simultaneously. The secondary apatite nucleation and growth depended on the rate of primary apatite nucleation. According to our results, moreover, the density of rutile nanorods can be newly considered to influence the ability to induce

the heterogeneous nucleation and growth of apatite. From the above discussion, we derived certain conclusions on apatite nucleation and growth on the surfaces of the rutile rod arrays on the CT-cpTi and CT-Ti6Al4V specimens, as follows:

- Active sites for primary apatite nucleation must be provided on the top surface of the rutile rods. These active sites consist of Ti–OH₂⁺ sites and Ti–O[−] sites on the rutile rods. The number of sites corresponds to the number of deposited hemispherical apatite particles on the surface.
- The rate of primary apatite nucleation and growth and the frequency of the nucleation must be dependent on the density of the active sites on the rutile rod arrays.
- The rate of secondary apatite nucleation and growth and the frequency of the nucleation must be dependent not only on the density of the active sites on the rutile rod arrays but also on the density of the rutile rods themselves. This secondary apatite nucleation and growth determine the diameters of hemispherical apatite particles.

Figure 7 illustrates apatite nucleation and growth on the rutile nanorod arrays on (a) CT-cpTi and (b) CT-Ti6Al4V specimens. According to Figure 6(a), the induction period for apatite formation extended in the order CT-cpTi < CT-Ti6Al4V. The changes in the diffraction peak area of apatite for the CT-Ti6Al4V specimens in Figure 6(a) indicated that the CT-cpTi substrate favors greater formation of apatite compared to the CT-Ti6Al4V specimen. The number of apatite particles (Figure 6(b)) indicated that the number of active sites for apatite nucleation on the CT-cpTi specimen was larger than that on the CT-Ti6Al4V specimen. As indicated in Figure 6(d), though the CT-cpTi and CT-Ti6Al4V specimens showed similar curves, the maximum number of apatite particles was greater on the surface of the CT-cpTi specimen. Such inactivation of apatite nucleation at an early stage may be a characteristic feature of CT-Ti6Al4V. The above findings indicate that the CT-Ti6Al4V specimen could not provide as many active sites for inducing apatite formation as the CT-cpTi specimen in SBF. As shown in Figure 1, a view from above shows the rod-like structures to be circular, and the densities of the rod-like structures approximately $(1.04 \pm 0.06) \times 10^3$ and $(0.70 \pm 0.10) \times 10^3 \mu\text{m}^{-2}$ for the CT-cpTi and CT-Ti6Al4V specimens, respectively. Although the widths of the nanorods on the CT-cpTi and CT-Ti6Al4V specimens were different, the sizes of nanorods on the two samples were closely similar (around 20 nm). The effective surface area of each rutile rod for producing active sites was ca. $3.14 \times 10^{-4} \mu\text{m}^2$. As seen in Figure 6(b), the number of active sites for apatite nucleation could be estimated when apatite particles covered the entire

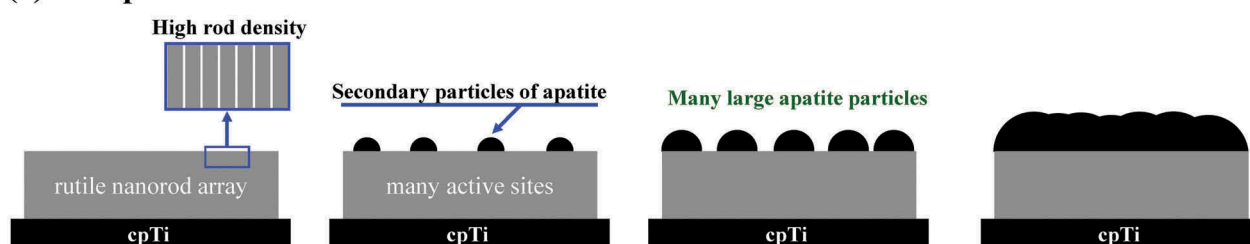
surface after 48 h of soaking in SBF. The densities of the active sites were ca. 0.16 and ca. 0.13 μm^{-2} on the CT-cpTi and CT-Ti6Al4V specimens, respectively. The possible relationship between the rutile rod density (per square micron) and active-site density (per square micron) is displayed in Table 1. We indicated that the rutile rod density on the surface varies by approximately $4.6 \times 10^4 - 6.9 \times 10^4$ (effective surface area: $14.44 - 21.66 \mu\text{m}^2$). This density is attributed to heterogeneous primary and secondary nucleation and growth of apatite and is possible a major determining the difference in apatite-forming ability. This indicates that the active-site density must increase as the density of the rutile rods increases.

In other words, rutile nanorod arrays on the CT-Ti6Al4V specimen involved fewer active sites for primary apatite nucleation. At an early stage, superior apatite nucleation occurs on the rutile arrays for the CT-cpTi substrate in supersaturated SBF owing to the high rod density on their surfaces. In Figure 6(b, c), the number and diameter of apatite particles increased with the soaking time in the range from 0 h to 40 h due to primary and secondary nucleation and growth of apatite. As indicated in Figure 6(d), rutile nanorod arrays on the CT-cpTi specimen were supposed to provide more active sites for primary apatite nucleation. This implies

Table 1. Relation between rutile rod density and active-site density for CT-cpTi and CT-Ti6Al4V specimens.

Sample	CT-cpTi	CT-Ti6Al4V
Rod density (μm^{-2})	$(1.04 \pm 0.06) \times 10^3$	$(0.70 \pm 0.10) \times 10^3$
Active-site density (μm^{-2})	0.16	0.13
Rods (per active site)	$6.1 - 6.9 \times 10^4$	$4.6 - 6.1 \times 10^4$

(a) CT-cpTi



(b) CT-Ti6Al4V

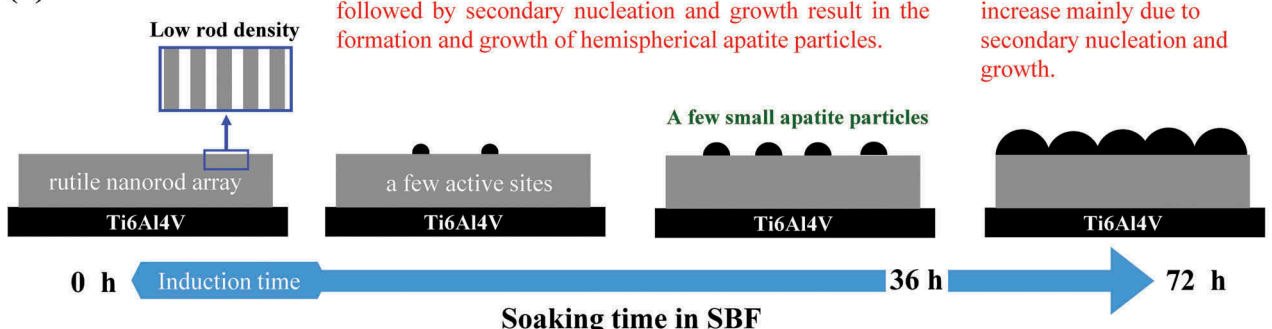


Figure 7. Schematic diagram of apatite nucleation and growth on rutile nanorod arrays of (a) CT-cpTi and (b) CT-Ti6Al4V specimens in SBF.

that a relatively large number of apatite nuclei are provided on the rutile rod array of the CT-cpTi specimens. These nuclei would accept more calcium and phosphate ions in SBF at the second stage of apatite growth. Thus, the large size of apatite secondary particles was attributed to the secondary nucleation and growth. The CT-cpTi specimen exhibited a stronger intensity of diffraction peaks corresponding to apatite after soaking in SBF for 72 h, as shown in Figure 4. This intensity could be attributed to the thick apatite layer on its surface. In addition, thick rutile layers were obtained on the surface of the CT-cpTi specimen, as shown in Figure 2(a). One possible explanation for the strong diffraction intensity of apatite is that thick rutile layers with high rod density provide more active sites for apatite formation.

In summary, highly ordered rutile nanorod arrays were synthesized on cpTi and Ti6Al4V alloys by chemical treatment and subsequent aging treatment. The rutile nanorod arrays exhibited an excellent ability to induce apatite formation. The superior apatite formation ability of the CT-cpTi specimen can be ascribed to the presence of a dense, thick rutile layer with high rod density.

5. Conclusions

Highly ordered rutile nanorod arrays were successfully prepared on the surfaces of cpTi and Ti6Al4V alloys by chemical treatment and subsequent aging treatment. The cpTi specimen favored the formation high-density rutile rods. Apatite particles were formed on the rutile nanorod arrays on the CT-cpTi and CT-Ti6Al4V alloy specimens by soaking the samples in SBF. However, the behavior of the apatite deposition on the two specimens was different. There were more deposited apatite particles on the CT-cpTi specimens than on the CT-Ti6Al4V alloy specimens after three days of soaking in SBF. The inferior ability to induce apatite nucleation on the CT-Ti6Al4V alloys at an early stage was due to the low density of rutile rods on the surface of the CT-Ti6Al4V alloy specimens, indicating that the amount of deposited apatite corresponded to the density of the rutile rods. Owing to the presence of a dense, thick rutile layer with high rod density on its surface, the CT-cpTi specimen showed superior apatite-forming ability to that of the CT-Ti6Al4V alloy specimens.

Acknowledgments

The authors are grateful to Dr. Noriyuki Nagaoka of Okayama University for his very kind assistance with the FE-SEM measurements of the CT-cpTi and CT-Ti6Al4V alloy specimens.

Disclosure statement

No potential conflict of interest was reported by the authors.

Funding

This research was partially supported by Grant-in-Aid for Challenging Exploratory Research Grant Number 24656386; Japan Society for the Promotion of Science [24656386]

References

- [1] De Groot K. Bioceramics consisting of calcium phosphate salts. *Biomaterials*. 1980;1(1):47–50.
- [2] Ohgushi H, Okumura M, Yoshikawa T, et al. Bone formation process in porous calcium carbonate and hydroxyapatite. *J Biomed Mater Res*. 1992;26(7):885–895.
- [3] Ong JL, Chan DCN. Hydroxyapatite and their use as coatings in dental implants: a review. *Crit Rev Biomed Eng*. 2000;28(5&6):667–707.
- [4] Harun WSW, Asri RIM, Alias J, et al. A comprehensive review of hydroxyapatite-based coatings adhesion on metallic biomaterials. *Ceram Int*. 2018;44(2):1250–1268.
- [5] Liu DM, Yang Q, Troczynski T, et al. Structural evolution of sol-gel-derived hydroxyapatite. *Biomaterials*. 2002;23(7):1679–1687.
- [6] Choi JM, Kong YM, Kim S, et al. Formation and characterization of hydroxyapatite coating layer on Ti-based metal implant by electron-beam deposition. *J Mater Res*. 1999;14(7):2980–2985.
- [7] Sun L, Berndt CC, Gross KA, et al. Material fundamentals and clinical performance of plasma-sprayed hydroxyapatite coatings: A review. *J Biomed Mater Res*. 2001;58(5):570–592.
- [8] Cho SB, Nakanishi K, Kokubo T, et al. Dependence of apatite formation on silica gel on its structure: effect of heat treatment. *J Am Ceram Soc*. 1995;78(7):1769–1774.
- [9] Kokubo T. Apatite formation on surfaces of ceramics, metals and polymers in body environment. *Acta Materialia*. 1998;46(7):2519–2527.
- [10] Kokubo T, Yamaguchi S. Simulated body fluid and the novel bioactive materials derived from it. *J Biomed Mater Res A*. 2019;107 A(5):968–977.
- [11] Kokubo T, Takadama H. How useful is SBF in predicting *in vivo* bone bioactivity? *Biomaterials*. 2006;27(15):2907–2915.
- [12] Shozui T, Tsuru K, Hayakawa S, et al. *In vitro* apatite-forming ability of titania films depends on their substrates. *Key Eng Mat*. 2007;330–332:633–636.
- [13] Shozui T, Tsuru K, Hayakawa S, et al. XPS study on potential suppression factors of suppressing *in vitro* apatite formation on anatase films prepared on various substrates. *Surf Coat Tech*. 2009;203(16):2181–2185.
- [14] Hayakawa S, Matsumoto Y, Uetsuki K, et al. *In vitro* apatite formation on nano-crystalline titania layer aligned parallel to Ti6Al4V alloy substrates with sub-millimeter gap. *J Mater Sci–Mater M*. 2015;26(6):190.
- [15] Hayakawa S, Masuda Y, Okamoto K, et al. Liquid phase deposited titania coating to enable *in vitro* apatite formation on Ti6Al4V alloy. *J Mater Sci–Mater M*. 2014;25(2):375–381.
- [16] Hayakawa S, Okamoto K, Yoshioka T. Accelerated induction of *in vitro* apatite formation by parallel alignment of hydrothermally oxidized titanium substrates separated by sub-millimeter gaps. *J Asian Ceram Soc*. 2019;7(1):90–100.

- [17] Liu X, Xiao F, Hayakawa S, et al. The fabrication of nanostructured titania polymorphs layer with high crystallinity and its apatite-forming ability. *Surf Coat Technol.* 2019;363:338–343.
- [18] Xiao F, Jiang GQ, Chen JY, et al. Apatite-forming ability of hydrothermally deposited rutile nano-structural arrays with exposed {101} facets on Ti foil. *J Mater Sci.* 2018;53(1):285–294.
- [19] Wu JM, Liu JF, Hayakawa S, et al. Low-temperature deposition of rutile film on biomaterials substrates and its ability to induce apatite deposition in vitro. *J Mater Sci–Mater M.* 2007;18(8):1529–1536.
- [20] Rohanizadeh R, Al-Sadeq M, Legeros RZ. Preparation of different forms of titanium oxide on titanium surface: effects on apatite deposition. *J Biomed Mater Res A.* 2004;71(2):343–352.
- [21] Liu X, Yoshioka T, Hayakawa S. Effect of titanyl sulfate concentration on growth of nanometer-scale rutile rod arrays on the surface of titanium substrate. *J Ceram Soc Jpn.* 2019;127(8):545–550.
- [22] Takadama H, Kim HM, Kokubo T, et al. XPS study of the process of apatite formation on bioactive Ti-6Al-4V alloy in simulated body fluid. *Sci Technol Adv Mat.* 2001;2:389–396.
- [23] Takadama H, Kim HM, Kokubo T, et al. TEM-EDX study of mechanism of bonelike apatite formation on bioactive titanium metal in simulated body fluid. *J Biomed Mater Res.* 2000;57(3):441–448.
- [24] Yamaguchi S, Hashimoto H, Nakai R, et al. Impact of surface potential on apatite formation in Ti alloys subjected to acid and heat treatments. *Materials.* 2017;10(10):1127.
- [25] Uchida M, Kim HM, Kokubo T, et al. Structural dependence of apatite formation on titania gels in a simulated body fluid. *J Biomed Mater Res A.* 2003;64A(1):164–170.
- [26] Li P, Ohtsuki C, Kokubo T, et al. The role of hydrated silica, titania, and alumina in inducing apatite on implants. *J Biomed Mater Res.* 1994;28(1):7–15.
- [27] Uetsuki K, Nakai S, Shirosaki Y, et al. Nucleation and growth of apatite on an anatase layer irradiated with UV light under different environmental conditions. *J Biomed Mater Res A.* 2013;101A(3):712–719.